



Piemsinlapakunchon, T. and Paul, M. C. (2018) Effects of content of hydrogen on the characteristics of co-flow laminar diffusion flame of hydrogen/nitrogen mixture in various flow conditions. *International Journal of Hydrogen Energy*, 43(5), pp. 3015-3033.
(doi:[10.1016/j.ijhydene.2017.12.103](https://doi.org/10.1016/j.ijhydene.2017.12.103))

This is the author's final accepted version.

There may be differences between this version and the published version. You are advised to consult the publisher's version if you wish to cite from it.

<http://eprints.gla.ac.uk/153994/>

Deposited on: 18 December 2017

Enlighten – Research publications by members of the University of Glasgow
<http://eprints.gla.ac.uk>

Effects of content of hydrogen on the characteristics of co-flow laminar diffusion flame of hydrogen/nitrogen mixture in various flow conditions

Tananop Piemsinlapakunchon and Manosh C. Paul*

Systems, Power & Energy Research Division, School of Engineering, University of Glasgow,
Glasgow, G12 8QQ, United Kingdom

*Corresponding author: Email: Manosh.Paul@glasgow.ac.uk

Tel: +44 (0)141 330 8466

Abstract

Effect of content of hydrogen (H_2) in fuel stream, mole fraction of H_2 (X_{H_2}) in fuel composition, and velocity of fuel and co-flow air (V_{avg}) on the flame characteristics of a co-flow H_2/N_2 laminar diffusion flame is investigated in this paper. Co-flow burner of Toro et al [1] is used as a model geometry in which the governing conservation transport equations for mass, momentum, energy, and species are numerically solved in a segregated manner with finite rate chemistry. GRI3 reaction mechanisms are selected along with the weight sum of grey gas radiation (WSGG) and Warnatz thermo-diffusion models. Reliability of the newly generated CFD (computational fluid dynamics) model is initially examined and validated with the experimental results of Toro et al [1]. Then, the method of investigation is focused on a total of 12 flames with X_{H_2} varying between 0.25 and 1, and V_{avg} between 0.25 and 1 ms^{-1} . Increase of flame size, flame temperature, chemistry heat release, and NOx emission formation resulted are affected by the escalation of either X_{H_2} or V_{avg} . Significant effect on the flame temperature and NOx emission are obtained from a higher X_{H_2} in fuel whereas the flame size and heat release are the result of increasing V_{avg} . Along with this finding, the role of N_2 and its higher content reducing the flame temperature and NOx emission are presented.

Keywords: Laminar diffusion flame; Hydrogen; Numerical modelling; Flame characteristics

1 Introduction

The demand for energy, which is increasing significantly, and the concern of environmental issues encourage the research and development in the various sectors of clean and sustainable energy. Among them, one of the attractive options is hydrogen (H_2) mixture fuel which can be produced by several methods (such as gasification, carbonization, steam reforming, and thermolysis), and also from flexible feedstocks (such as coal, wood and biomass). Research and development relating to this fuel, which is considered to be environmentally friendly and sustainable, has been focused on both the production techniques and the possibility of replacing the conventional carbon fuel used in various combustion systems. Since different methods are employed for the production of H_2 mixture fuel, the composition of H_2 mixture fuel is varied and depends strongly on the production technique and feedstock. Fuel composition could be a mixture of H_2 , which is a major fuel component, with other species such as carbon monoxide (CO), carbon dioxide (CO_2), nitrogen (N_2), and methane (CH_4) at different percentage of volume or mass. This variation thus points to the necessity of understanding the microscopic processes governing the combustion characteristics of this fuel.

Diffusion flame is selected as a source of heat energy in several applications and, characteristics of this flame were presented in the literature. A summary of the papers relating to the flame characteristics of H_2 mixture and H_2 /hydrocarbon fuel is presented in Table 1. In those papers, the effect of the content of H_2 in fuel composition on the flame characteristics was examined through diffusion flame generated by a counter-flow or co-flow configuration at various strain rates and flow regimes. A large number of research papers paid attention to the turbulent flame whereas the work focusing on the laminar flame is limited. Flame structure, temperature and species profile were studied by the numerical and experimental methods. And the topics of interest could be categorised as: (i) the effect of adding H_2 content to hydrocarbon fuel, (ii) the effect of H_2 content on the flame characteristics of H_2 mixture fuel, and (iii) the effect of chemistry reaction mechanisms of H_2 mixture fuel.

In the first category, increasing stability and reducing CO emission were expected to be the result of adding H_2 content into the composition of hydrocarbon fuel since a lower content of hydrocarbon was supplied into combustion. This expectation was achieved in [2], [3], [4], and [5] where the flames of H_2 /hydrocarbon e.g. H_2/C_3H_8 , H_2/CH_4 , and H_2 /natural gas with different X_{H_2} were studied. Nevertheless, the addition of H_2 content also affected the

characteristics of flame strongly. For example, the flame dimension was reduced whereas the NO_x and soot emission formulations resulted at a higher rate than a conventional hydrocarbon fuel. Moreover, the faster burning rate along with the higher flame temperature due to the role of H₂ in combustion was the cause of this effect.

With regard to the H₂ mixture fuel, the role and effect of the H₂ content on the diffusion flame characteristics were studied in several research papers. Attention was paid to the flame structure, temperature, and species distribution profiles. Syngas (H₂/CO) and syngas with the dilution of N₂, CO₂, and H₂O diffusion flame generated by a counter-flow burner were also studied in [6] and [7], while the syngas and the H₂/N₂ turbulent flame formulated by a co-flow burner were examined in [8]. A similar result was obtained from both the burner configurations. In terms of the temperature of both the syngas and H₂/N₂ flames, fuel containing a higher content of H₂ formulated a higher flame temperature. Additionally, the flame dimension was found to be larger and more affected by the content of H₂ than for syngas and H₂/N₂, which is in contrast to an enrich CO flame.

The chemical reaction mechanisms capable of computing combustion of H₂ mixture fuel have been studied and presented in a number of research papers. Majority of them focused on the combustion of syngas (H₂/CO). However, the mechanisms presented have the potential to predict the reactions of a H₂ mixture fuel since the various species were taken into account [9] and [10]. In addition, a review and comparison of the various reaction mechanisms have been presented in [11] with the aim of finding the most suitable chemical mechanism compositions for predicting and explaining the syngas combustion. A total of 16 recent mechanisms such as GRI3 [12], K romn s-2013 [13], Davis-2005 [14], Li-2007 [15], Burk-2012 [16] and NUIG-NGM-2010 [17] can also provide a good prediction of computational result with experiment; however, the level of accuracy of each mechanism strongly depends on the condition of combustion (e.g. pressure and temperature) and in fact, some mechanisms have a limitation in terms of the number of species. Similarly, 3 reaction mechanisms (GRI 3.0, DRM22 [18] and Heghes' C1–C4 [19]) seemed to be capable of computing a mixture of H₂ flame with CH₄, CO, CO₂, H₂ and H₂O, since a good agreement with the experimental data was obtained from these mechanisms [20].

However, in order to use a H₂ mixture fuel effectively, understanding the effect of H₂ content in fuel – which is defined in this study by the volume flow rate of H₂ to be supplied into the combustion - on the flame characteristics is a significant step towards the better utilisation of

the hybrid hydrogen mixed fuels. The investigation is focused on a combination of the varying mole fraction of H₂ (X_{H_2}) in fuel composition, and the velocity of fuel and co-flow air (V_{avg}). Therefore, not only the effects of H₂ content but also V_{avg} and X_{H_2} are examined in this paper. In particular, the aim of the work is focused on how the H₂ content affects the flame characteristics of the H₂/N₂ laminar co-flow diffusion flame. This also includes an in-depth investigation of the flame structure, flame temperature, species distribution, and NO emission formation at the various concentration of H₂ in fuel.

Computational fluid dynamics (CFD) commercial code ‘STAR CCM+’ is selected as a tool for simulating and studying the flame. Suitable chemical reaction mechanisms including its thermodynamic and transport data sourced from the literature are imported to the generated numerical models. However, as the computational time for simulating the finite rate chemical kinetics reactions incorporated in the species transport models depends strongly on the number of species and reactions involved in the reaction mechanisms, an optimum computational setup is thus crucially important for obtaining the reliable numerical results with a reasonable computational time. Validation of the generated model is processed in the first stage then the content of H₂ in the fuel composition is varied at a different velocity of fuel and air in order to study the effect of the H₂ content at different flow conditions. We believe that the results presented in the paper would be beneficial in terms of the design and selection of a combustion system that can combust a H₂ mixture fuel efficiently with a low rate of pollution formation.

2 Model formulation

The selected configuration is an axisymmetric co-flow burner as presented in Toro et al [1]. Appearance and geometry of this burner are shown in Figure 1. The fuel inlet is a round tube located at the centre with an inner diameter of 9 mm. This inlet is surrounded by a 95 mm inner diameter co-flow air inlet. The thickness of the fuel tube is defined as 1 mm and the position of the fuel exit is 8 mm higher than that of the co-flow air. Both fuel and air are injected vertically in the opposite direction to the gravitational force.

2.1 Governing equations

The governing equations are presented as follows:

Continuity equation

$$\frac{\partial \rho}{\partial t} + (\rho \vec{V}) = 0 \quad (1)$$

Momentum equation

$$\frac{\partial(\rho\vec{V})}{\partial t} + \nabla \cdot (\rho\vec{V}\vec{V}) = -\nabla p + \nabla \cdot \vec{\tau} + \rho\vec{g} \quad (2)$$

Where

$$\vec{\tau} = \mu[\nabla\vec{V} + \vec{V}^T - \frac{2}{3}\nabla\vec{V}I]$$

Species transport equation

$$\frac{\partial(\rho Y_i)}{\partial t} + \nabla \cdot (\rho\vec{V}Y_i) = -\nabla\vec{J}_i + R_i + S_i \quad (3)$$

Energy equation

$$\nabla \cdot (\vec{v}(\rho E + p)) = \nabla \cdot (k\nabla T - \sum_j h_j\vec{J}_j + (\vec{\tau} \cdot \vec{v})) + S_h \quad (4)$$

Where

$$E = h - \frac{p}{\rho} + \frac{v^2}{2} \quad \text{and} \quad h = \sum_j Y_j h_j$$

Multi-component diffusion as well as thermal diffusion is considered as shown in (5). The previous one is computed through the Maxwell-Stefan equation while the latter is by the Warnatz model. Details of these methods can be found in [21] and [22].

$$\vec{J}_i = -\rho \left(\sum_{j=1}^N D_{i,j} \nabla Y_j \right) - \rho \frac{D_{T,i}}{T} \nabla T \quad (5)$$

The dynamic viscosity and thermal conductivity are defined by the Chapman-Enskog method and kinetic theory respectively. These are illustrated in (6) and (7) respectively

$$\mu_i = 2.6693 \times 10^{-6} \frac{\sqrt{M_i T}}{\sigma_i^2 \Omega(T^*)} \quad (6)$$

$$\lambda_i = \frac{\mu_i}{M_i} (f_{tran} C_{v,tran} + f_{rot} C_{v,rot} + f_{vib} C_{v,vib}) \quad (7)$$

Participating media radiation model is selected for computing radiation. Discrete Ordinates Method (DOM) is utilized for solving the radiation transport equation [21]. The absorption coefficient is calculated through the weighted sum of grey gas model (WSGG). The total absorptivity of several grey gases is approximated as shown in (8). The medium is assumed to consist of different fractions of grey gases with different absorption coefficients. CO₂ and H₂O are assumed to dominate the cloud emission and absorption among the combustion gas products.

$$\alpha \approx \sum_{k=0}^K a_k (1 - e^{-K_k S}) \quad (8)$$

The medium is also assumed to be optically thin. Thus, the optical path length (S) is defined as:

$$S = 3.6 \frac{\text{Volume of the domain}}{\text{surface area of domain}} \quad (9)$$

The GRI3 reaction mechanisms containing 53 species and 325 reactions are selected and the governing equations are solved by using the numerical techniques presented in Section 2.3.

2.2 Boundary conditions and mesh generation

The domain is axisymmetric and considered volume above the co-flow air and fuel inlet, as shown in Figure 1. The width of the top plane is 4.75 cm. This distance is accounted from the centreline of the fuel tube to the outer line of the co-flow air tube horizontally. The width of the bottom plane is 4.2 cm and is between the outer of the co-flow air and the outer of the fuel tube. The distance between the top and bottom planes is 20 cm and the thickness of the fuel tube is assumed as 1 mm. Fuel inlet width/radius is 0.45 cm from the centreline and is located 0.8 cm above the air inlet. According to this setup, the effect of the fuel tube on the flow of the co-flow air due to the different level between the co-flow air inlet and fuel inlet (8 mm) is taken into account.

Regarding the boundary condition, the top and left planes are defined as a pressure boundary with the temperature and total pressure of 298 K and 101325 Pa respectively. Species on these boundaries is air which is defined in terms of the mole fraction of O_2 and N_2 . Fuel and the co-flow air inlet are set as a velocity inlet boundary. A parabolic velocity profile is defined for the fuel injection while a bulk velocity profile is specified for the co-flow air. Both streams are supplied into the domain at an initial temperature of 298 K. The centreline of the fuel tube or the right plane is the axis of the domain. The fuel tube and its thickness are defined as a wall boundary with a no-slip condition and temperature of 298 K. All the boundary setup of each plane is illustrated in Figure 1.

Using a hyperbolic function, a clustering mesh is generated with the grids stretching both vertically and horizontally from the outer of the fuel tube to the top and left pressure outlet planes, axis, and co-flow air inlet. This mesh generation is designed for computing the reacting flow field as well as the fluid interaction between the fuel inlet tube and the co-flow air stream. Mesh size with the number of cells is optimised from a mesh sensitivity test carried out through the three levels of mesh resolution. The smallest cell size of the selected mesh resolution (normal mesh) is 0.2 mm and is located at the outer of the fuel inlet tube. The

number of divisions in the vertical direction is 100 and 24 from the smallest cell position to the top plane and co-flow inlet respectively. In the horizontal direction, 50 and 16 divisions are produced from the smallest cell location to the left outlet plane and axis. Thus, a total of 7,800 mesh cells are produced based on this setup. This mesh generation is illustrated in Figure 1 whereas the details of the other mesh resolution study (fine and coarse mesh) are presented in Table 2.

2.3 Numerical techniques

The continuity, momentum, species transport, and energy equations are solved in a segregated manner. In order to formulate the species transport equation, an ‘operator splitting’ algorithm is also utilised. This algorithm, which is inbuilt in the selected commercial package, takes advantage of the different time scales involved in the chemical reactions and the flow field [21]. The reaction rates and complex chemistry problem are solved by the Sundials CVODE ODE solver developed and introduced by [23]. The temperature of cells close to the fuel and air exit is set at 1800 K for the first 20 iterations in order to ignite the flame. The simulation was then run until the convergence is obtained with a steady-state profile of the contour plots of the velocity, temperature and concentration of major species (H_2 , N_2 , O_2 , N_2 , H_2O , NO and NO_2). Residuals of the continuity, momentum, and energy equations are resulted between 10^{-4} and 10^{-6} and remained to be stable thus ensured the solution stability and steadiness.

The numerical simulations are processed in two stages. A validation of the generated CFD model based on the experimental and numerical data of Toro et al [1] is presented first in Section 3, while the study investigating the effects of the content of H_2 , X_{H_2} , and V_{avg} on the flame characteristics in various flow conditions is in the second stage (Section 4).

3 Validation of the modelling results

In this stage, the simulation cases are run at the similar flow condition and fuel composition as in Toro et al [1] in order to validate the simulation results with their experimental data. The mole fraction ratio of $H_2:N_2$ is kept constant at 1:1. In each of the test cases, the average velocity of the fuel and air (V_{avg}) are defined equally to 0.27 ms^{-1} for one case and 0.5 ms^{-1} for the other case to study the effect of V_{avg} on the flame characteristics [1]. A user defined function (UDF) is written to define a parabolic velocity profile of fuel at the burner inlet. Computational results are compared with the experimental as well as the numerical result of

Toro et al. [1] in Figure 2-3 which respectively present the axial temperature and species profiles of both the flames ($V_{avg} = 0.27$, and 0.5 ms^{-1}) and the radial temperature and species profiles of the flame at $V_{avg} = 0.5 \text{ ms}^{-1}$.

As seen, at 0.5 ms^{-1} , the axial temperature is slightly overpredicted by the model and the maximum temperature computed is approximately 50 K higher than that of the experiment. However, this result has a trend similar to the CFD result of Toro et al [1] which also overpredicted the temperature profile. The maximum temperature of the simulated flame is located at the similar position to the experimental data due to the good prediction of the flame length and flame front. This is also supported by the computational result of the species profile of H_2 , N_2 , O_2 , and H_2O which are comparable to the experimental data.

On the radial plot, at 3 mm above the fuel inlet, the slightly over prediction also results from the simulation model. This is, again, very similar to the CFD result of Toro et al [1]. However, the position of the maximum temperature and the thickness of the high temperature zone (above 298 K) results closer to the experimental data. This further implies the good prediction of the flame dimension at this height above the burner. Species distribution results are similar between the experiment and the newly generated CFD models. However, slightly under prediction is shown at the radial distance greater than 5 mm in the profiles of H_2 and H_2O and slightly over prediction is shown between 7.5 – 8.5 mm radial distances for the species of O_2 . Nevertheless, this can be considered as insignificant.

At 10 mm above the fuel inlet, well prediction is also obtained from the generated CFD model on both the radial temperature and species profiles with a slightly over prediction at distances less than 2.5 mm for H_2 and between 5 – 6.5 mm for H_2O . However, this is also not considered as significant. The thickness of the high temperature zone is predicted to be slightly thinner than that of the CFD result of [1] while the species profiles predicted by both the models are similar.

Similar temperature and species profile as at 10 mm are obtained at 20 and 30 mm above the fuel inlet. Generally, the presented model produces the results similar to those of the experiment. Though slightly over or under prediction are obtained for the H_2 and N_2 profiles with a resulting slightly wider high temperature zone, the majority of these profiles are comparable to the experimental data. Also, the location of the predicted peak temperature in

the radial distance, which is similar to the experimental data, further emphasises the good prediction of the flame dimension.

Going back to the axial plot of the flame temperature presented in Figure 2(a) at a reduced flow velocity $V_{avg} = 0.27 \text{ ms}^{-1}$, it is seen that the temperature is also slightly over predicted. But the location where the peak temperature occurred is similar to the one resulted from the CFD model of Toro et al. [1]. Furthermore, the species profile is well predicted and is also comparable to the one computed by Toro et al. [1].

Mesh dependency test is also carried out along with the validation routine and presented in Figure 4. The same direction of the result is shown from the comparison of the flames generated using the three different mesh resolutions. Almost the same temperature and the species profiles are predicted from the medium and fine mesh resolutions. But, slightly overprediction in the axial temperature towards the downstream of the burner is shown from the coarse mesh. Thus, the medium mesh resolution is to be considered for the further simulations since it provides the result similar to that obtained by the fine mesh but with less computational time.

4 Effects of content of H₂ on the flame characteristics

The content of H₂ defined as the flow rate of H₂ in the fuel stream is varied in order to study its effect on the diffusion flame characteristics. This can be processed by varying either or both of (i) the concentration of H₂ in fuel (X_{H_2}), and (ii) the velocity of fuel and air (V_{avg}). Therefore, 12 flames having various X_{H_2} (0.25 - 1 in the mole fraction) and V_{avg} (0.25 - 0.75 ms^{-1}) are simulated. Following this setup, 3 pure H₂ flames ($X_{H_2} = 1$) having various V_{avg} are also generated. This is proceeded with the aim of comparing characteristics between the H₂/N₂ and pure H₂ flames. Details of fuel supplied for generating these flames such as the flow velocity, fuel composition, and content of each species supplied into combustion are shown in 3. Characteristics of these flames are studied by considering various aspects such as the flame structure, flame temperature, chemistry heat release, species distribution, and NO_x emission.

Regarding X_{H_2} and V_{avg} , an analysis of the effect of X_{H_2} is processed by studying the flames formulated by the same V_{avg} but with different compositions (different X_{H_2}). On the other hand, the comparison of flames generated by the same composition (same X_{H_2}) but with different V_{avg} is proceeded in order to identify the effect of V_{avg} . To prevent any confusion

and simplify the analysis, the simulated flames are categorised based on the X_{H_2} and V_{avg} of their fuel stream. Flames generated based on the same fuel composition (i.e. the same X_{H_2}) but with different V_{avg} are grouped as an enrich N₂ flame ($X_{H_2} = 0.25$), equal H₂/N₂ flame ($X_{H_2} = 0.5$), enrich H₂ flame ($X_{H_2} = 0.75$), and a pure H₂ flame ($X_{H_2} = 1$). Effect of V_{avg} is identified through the separate study of each flame group. In contrast, the flames generated by fuel having the same V_{avg} are categorised into three flame sets for studying the effect of X_{H_2} . These are flame set I ($V_{avg} = 0.25 \text{ ms}^{-1}$), flame set II ($V_{avg} = 0.5 \text{ ms}^{-1}$), and flame set III ($V_{avg} = 0.75 \text{ ms}^{-1}$). Category of all the flames studied is presented in Table 4.

4.1 Flame appearance

Temperature contours of all the enrich N₂ and enrich H₂ flames (flames A, C, E, G, I, and K) are presented in Figure 5. Zero temperature gradient method is applied on the temperature contour of all the flames in order to illustrate the flame front line which is capable of projecting the flame appearance and its dimension. The dimension, maximum flame width, as well as the length of all the flames extracted from the flame front line, are presented and compared each other in Figure 6 and Figure 7a. These results are used to compute the vertical cross sectional area of all the flames and, by integrating this area around the axis of the domain results in the flame size. Comparison of the flame size of all the flames is shown along with the H₂ content in the fuel stream in Figure 7b. Moreover, the results presented in Figures 5 – 7 are used for identifying the effects of the H₂ content, X_{H_2} , and V_{avg} on the flame appearance and discussed below.

As seen in Figure 6, the shape of all the flames is similar and is almost downward parabolic. The flame front line illustrating the flame shape begins at the outer of the fuel exit, which passes through the axis and finishes on the other side of the outer fuel exit tube. Different flame size and dimension are found from the analysis and summarised in Figure 6 – 7. The largest flame size is found in flame L (i.e. pure H₂ flame with $V_{avg} = 0.75 \text{ ms}^{-1}$) as 14.6 cm^3 , followed by flame K (i.e. enrich H₂ flame with $V_{avg} = 0.75 \text{ ms}^{-1}$) as 10.4 cm^3 whereas the smallest one is resulted from flame A (enrich N₂ flame with $V_{avg} = 0.25 \text{ ms}^{-1}$) as 1.39 cm^3 . Thus, this elucidates the content of H₂ playing a significant role on the flame size. Further, a relationship between them tends to be directly proportional. Interesting result is also found while comparing the flames generated by the fuel containing the same content of H₂ (keeping the same volume flow rate of H₂) e.g. (i) flames B and E, (ii) flames C and I, (iii) flames D and F, and (iv) flames G and J. In these comparisons, the flames generated by the fuel

containing higher X_{H_2} have a smaller flame size for (i), and (ii) but a larger flame size for (iii) and (iv).

An understanding of the combined effect of X_{H_2} and V_{avg} is developed and presented by considering the flame set I, II, and III separately. Generally, the fuels consisting higher X_{H_2} generate the flame larger than the ones containing lower X_{H_2} . However, the relationship between them is highly non-linear with an average increasing rate of 2.84, 6.09, and 9.31 cm³ per increment of X_{H_2} from 0.25 as illustrated in Figure 7b. Similar relation is also resulted for V_{avg} i.e. the flame size, computed from all the enrich N₂ flames, equal H₂/N₂ flames, enrich H₂ flames, and pure H₂ flames, resulted in the increase of 1.7, 2.65, 3.64, and 4.95 cm³ respectively as shown in Figure 7b for per increment of $V_{avg} = 0.25$ ms⁻¹.

With regard to the flame dimension, an analysis of the maximum flame width and flame length is carried out and results are presented in Figure 7a with an effect of the H₂ content, X_{H_2} , and V_{avg} . The highest and lowest maximum flame width of 1.7 and 1.05 cm is obtained from flames L and A respectively. Profiles of the maximum flame width and the H₂ content are similar. However, a relation between them cannot be easily formulated since some flames generated by the fuel having lower H₂ content form a wider maximum flame length i.e. flames C and F. Nevertheless, a strong effect of X_{H_2} on the maximum flame width is pointed out with an average increasing rate per increment of $X_{H_2} = 0.25$ as 0.160 cm for flame set I, 0.186 cm for flame set II, and 0.214 cm for flame set III. Effect of V_{avg} on the maximum flame width can be considered as weak, since its rate of increment is only 0.004, 0.051, 0.064, and 0.085 cm respectively per increment of V_{avg} from 0.25 ms⁻¹.

In terms of the flame length, Figure 7a also shows flame L (pure H₂ flame with $V_{avg} = 0.75$ ms⁻¹) having the longest length and it is ~9.74 cm while the shortest flame length is flame A (enrich N₂ flame with $V_{avg} = 0.25$ ms⁻¹) as 2.74 cm. On the other hand, considering the H₂/N₂ flames, flame K (pure H₂ flame with $V_{avg} = 0.75$ ms⁻¹) has the longest flame length as 8.75 cm and each flame set is unique and solely results in the effect of X_{H_2} on this parameter. However, the flame generated by the fuel consisting higher X_{H_2} is slightly longer and an average increasing rate is computed to be 0.46, 0.51, 0.58 cm for the flame sets I, II, and III respectively. Significant effect is also found when increasing V_{avg} . For example, the fuel stream having a higher V_{avg} produces a longer flame with an escalating rate for per increment

of V_{avg} at every 0.25 ms^{-1} : 2.62 cm for the enrich N_2 flames, 2.56 cm for the equal H_2/N_2 flames, 2.69 cm for the enrich H_2 flames, and 2.81 cm for the pure H_2 flames.

4.2 Flame temperature

In all the flames, the position of the maximum flame temperature is obtained on the flame front line slightly above the outer of the fuel exit tube as can be seen in the temperature contour (Figure 5). To clearly illustrate the effect of the H_2 content, X_{H_2} and V_{avg} on this position, the solid circles are plotted on the flame front line as shown in Figure 6. As seen, the location of the maximum temperature depends on the H_2 content with having a direct proportion relation. In fact, the position of the maximum temperature has a higher vertical distance from the fuel exit, and a longer horizontal distance from the axis, when the H_2 content supplied was large. Thus, the X_{H_2} plays an important role when the flames supplied by the same content of H_2 are compared. Analysing flames in the flame sets I, II, III, a direct proportion relation can also be obtained for all the flame sets. For example, higher vertical distance from the fuel exit, and longer horizontal distance from the axis are resulted when the fuel containing higher X_{H_2} is compared with the lower one. Similar direction of result is found when V_{avg} is escalated. For example, higher V_{avg} provides the higher vertical distance and also the longer horizontal distance in all the N_2 flames, equal H_2/N_2 flames, enrich H_2 flames, and pure H_2 flames.

Apart from the position, the maximum temperature of all the simulated flames is also presented and compared with their adiabatic flame temperature in Figure 8a. The highest flame temperature results from flame L (pure H_2 flame with $V_{avg} = 0.75 \text{ ms}^{-1}$) as 2319 K while the lowest one is found from flame A (enrich N_2 flame with $V_{avg} = 0.25 \text{ ms}^{-1}$) as 1552 K. Generated H_2/N_2 flame having the highest maximum flame temperature is flame K (2193 K). Maximum flame temperature of the simulated flames is found to be lower than the adiabatic temperature except for the enrich N_2 flames. The average difference between the adiabatic and simulated flames are shown to be 36 K for the rich N_2 flame, 68 K for the equal H_2/N_2 flame, 96 K for the rich H_2 flame, and 91 K for the pure H_2 flame. These are computed from the flames formulating by the fuel having the same composition but with different V_{avg} .

However, as shown in the same figure, an escalation of the H_2 content (volume flow rate of H_2) does not affect the maximum flame temperature directly. There are some cases that the flame generated by the fuel stream with lower H_2 content have the maximum temperature

higher than that of the one generated by the fuel stream having a higher one. Considering the flames in the same flame set points to the stronger effect of X_{H_2} on the maximum flame temperature. The average increasing rate per increment of $X_{H_2} = 0.25$ is found to be 231, 243, 249 K for the flame sets I, II, and III respectively. Slightly increase of the maximum flame temperature is shown when the flame generated by the fuel having the same composition but with different V_{avg} . With an increase of V_{avg} as 0.25 ms^{-1} , the maximum flame temperature of the enrich N_2 flame, equal H_2/N_2 flame, enrich H_2 flame, and pure H_2 flame escalates to 10, 34, 39, and 37 K respectively in average.

4.3 Chemistry heat release and heat flux generated by the flames

The finite rate chemistry implemented in the model provides the capability of calculating the heat release as presented in Figure 8b. The lowest value of 48 W among all the simulated flames is found in flame A (N_2 rich flame with $V_{avg} = 0.25 \text{ ms}^{-1}$) whereas the highest value of 514 W is computed from flame L (pure H_2 with $V_{avg} = 0.75 \text{ ms}^{-1}$). For the H_2/N_2 flames, the highest chemistry heat release of 375 W is resulted from flame K. Similar to the relation between the maximum temperature and the H_2 content presented in the previous section, a relationship between the chemistry heat release and the H_2 content is also established.

Generally, higher H_2 content provides higher chemistry heat release. This finding is supported by the high calorific value of H_2 . But specifically, an average increasing rate of the chemistry heat release of flame sets I, II, and III is obtained as 56, 91, and 130 W per increment of $X_{H_2} = 0.25$. Effect of V_{avg} on the chemistry heat release of the flames is also clear – with an average increasing rate of every 0.25 ms^{-1} it is (i) 40 W for the N_2 rich flame, (ii) 75 W for the equal H_2/N_2 flame, (iii) 110 W for the H_2 rich flame, and (iv) 150 W for the pure H_2 flame.

In terms of the heat flux, a profile of this parameter on the left pressure outlet boundary is plotted in Figure 9a-c for every flame and it is found to be dominated by the radiative heat flux. The profile of the heat flux on the left plane is similar in all the flames, and it increases to the peak value then reduces along the vertical distance. The relation between the peak value and the H_2 content supplied cannot be identified directly as some fuels with lower H_2 content in the fuel stream generate higher peak heat flux on the boundary. Considering the effect of X_{H_2} , higher X_{H_2} provide more heat flux generated in combustion. This finding can be seen in all the flame sets where the flames generated by the fuel containing $X_{H_2} = 1$ (pure H_2) produce the highest heat flux. Moreover, escalation of V_{avg} itself also provides more chemistry heat release, as higher value is found from the flames having the same composition

but with higher V_{avg} . However, among all the simulated flames, the highest heat flux is resulted from flame L (pure H₂ flame and $V_{avg} = 0.75 \text{ ms}^{-1}$) with the peak value of 1528 W/m² while the lowest one is resulted from flame A (enrich N₂ flame with $V_{avg} = 0.25 \text{ ms}^{-1}$) with the peak value of 11.42 W/m². The highest heat flux among the H₂/N₂ flames is computed from flame K (enrich H₂ flame with $V_{avg} = 0.75 \text{ ms}^{-1}$) as 859 W/m².

4.4 Species distribution

Species profiles of H₂, N₂, O₂, and H₂O are studied in this section. Axial species of all the H₂/N₂ flames at different V_{avg} are presented in Figure 10a-d whereas the radial species profiles of the selected ones are presented in Figure 11a-d. For the radial profiles, all the simulation flames are monitored at 9 mm above the fuel exit.

As a major fuel component, H₂ is consumed along the axial distance from the fuel exit, as a results the chemistry reactions related to H₂ convert this reactant to other product species. In the H₂/N₂ flames, the position where H₂ is fully consumed is slightly under the flame front, and noticeably, the position of the flame front and dimension are different and they strongly depend on the X_{H_2} and V_{avg} . Moreover, the H₂ mole fraction with higher X_{H_2} approaches zero at a position higher than that with lower X_{H_2} . On the radial plot, the concentration of H₂ is reduced along the radial distance and approaches zero before the flame front line, similar to its axial profile.

Regarding the mole fraction profile of N₂, which is supplied into the reactions through both the streams, fuel and oxidizer, the concentration of this species increases along the axial and radial distances from the fuel inlet and axis. On the axial plot, this escalation is significant and tends to approach 0.79 of the mole fraction which is the same value of the concentration of N₂ in the air stream. The slightly different profile can be seen in the H₂ rich and equal H₂/N₂ flames; for example, the concentration of N₂ rises to their peak value approximately 0.81 and 0.91 respectively for the equal H₂/N₂ flame (flame B, F, and J), and for the rich H₂ flame (flame C, G, and K). It then slightly reduces to approximately 0.79. The escalation of the mole fraction of N₂ on the radial plot is obtained similarly. Significant increase along the radial distance is shown and again tends to 0.79. The slightly different profile is found in flame A, B, and C (flames in the flame set I). For instance, the N₂ profile of these flames rises to the peak value at 0.86, 0.83, and 0.82 in order, and then slightly decreases to 0.79. This finding thus clarifies that the level selected for monitoring the radial profile is higher than the

position of the maximum temperature of the flames in flame set I. Since N_2 is not fully consumed during combustion, the concentration of this species increases and approaches the same concentration of N_2 in air when it is outside the reaction zone. The fluctuation of N_2 concentration observed is the resultant effects of the combination of N_2 supplied through both the air and fuel streams which can therefore lift the concentration of this species higher than the one in the case of only air (0.79).

As an oxidizer, O_2 is supplied through the air stream and fully combusted at the area close to the flame front. This is supported by the axial and radial profiles of this species which appear on the plot at the position close to and inside the flame front line on both the axial and radial plots. It can be seen that the profile of O_2 is strongly affected by X_{H_2} and V_{avg} since these parameters are capable for controlling the dimension of the flame as well as the flame front line. The O_2 concentration increases until approaching 0.21 of the mole fraction which is the concentration of this specie in the air stream. The increasing rate of the mole fraction profile of O_2 is found to have the similar values. This result can also be seen on both the axial and radial plots where almost the parallel profile of O_2 of all the flames is shown.

However, as a reaction product, the concentration of H_2O increases from zero to the peak value then reduces to zero again. The position of the peak value is close to and inside the flame front. The peak concentration of all the flames is obtained differently. The highest peak value obtained from flame C is 0.28 and 0.28 on the axial and radial plots respectively. Conversely, the lowest peak value found in flame A is 0.13 and 0.15 from the axial and radial plots in order. It is also noticed from both the plots that the flames having the same composition (flame set I) have the higher peak value than that of the sets II, and III.

4.5 NOx emission

Utilisation of the GRI3 reaction mechanisms allowed the prediction of the NOx emission in the flames and, the concentration and production rate of NOx are the key focus of the investigation. Note that the concentration is defined by the summation of the concentration of NO and NO_2 on the each computational grid.

The appearance of the contours of the NOx concentration presented in Figure 12 is similar to the flame temperature (Figure 5), thus indicating the NOx emissions resulted from the thermal route. Maximum concentration along with the maximum flame temperature is also plotted in Figure 13a in order to investigate the role of NOx against the temperature in details. As can be seen, the flame temperature has a significant role and effect on the NOx

resulted. Generally, the fuel that is capable of producing the higher flame temperature generates the higher NO_x concentration. Thus, all the factors affected the escalation of the flame temperature also imply here, and consequently increase the NO_x concentration. Quantitatively, the highest NO_x concentration of all the flames (295.35 ppm) is found from flame L, whereas the highest concentration of the particularly H₂/N₂ flames (132.07 ppm) is resulted from flame K. Conversely, the lowest concentration is computed from flame A as 11.13 ppm.

Effect of the H₂ content, X_{H_2} , and V_{avg} on the NO_x concentration is also quantified. For example, an average increase of 72.67, 100.33, and 120.60 ppm respectively from the flame sets I, II, and III is resulted per increment of X_{H_2} as 0.25. Whereas, it is 11.98, 37.48, 107.03, and 236.32 ppm respectively from the enrich N₂ flame, equal H₂/N₂ flame, enrich H₂ flame, and pure H₂ flame per increment of V_{avg} as 0.25 ms⁻¹.

The NO_x production rate of all the flames is also presented in Figure 13b. This result is calculated by integrating the summation of the production rates of NO and NO₂ on all the grids around the domain. As observed, a significant effect of X_{H_2} is discovered. For instance, the fuels having a higher X_{H_2} formulate the NO_x production at higher rate than the lower one. This result is obtained not only from the consideration of the flames in the same flame set but also from the comparison of all the flames. The average increasing rate is found as 2.99, 4.83, 6.28 kg-m⁻³s⁻¹ per an increment of $X_{H_2} = 0.25$ for the flame sets I, II, and III respectively.

Effect of V_{avg} on the flame is also discovered from the analysis of the flames generated by the fuel having the same composition. However, an increase of V_{avg} results in slightly increase of the NO_x production rate. The average increasing rate of the NO_x production due to the alternation of V_{avg} is calculated for the enrich N₂ flame, equal H₂/N₂ flame, enrich H₂ flame, and pure H₂ flame in order as 0.47, 2.17, 5.43, and 10.72 kg-m⁻³s⁻¹.

While comparing the results of the NO_x emission with the chemistry heat release reported in the previous section, it is interesting to note the fact of discovery that some flames formulated a lower rate of NO_x formation though generating the higher chemistry heat release. Thus, this clearly points to the methods capable of reducing the NO_x emission while maintaining the heat release at an expected level. The findings support the flames with reducing X_{H_2} and increasing V_{avg} have this beneficial impact. Nevertheless, a larger flame size would be the side effect of this method.

5 Discussion

The slight differences appeared between the CFD results of [1] and the ones generated in this work can be further explained by considering a number of factors. Firstly, the species properties such as the dynamic viscosity, molecular diffusivity, thermal conductivity, and thermal diffusion are defined by different methods. Secondly, the fluid interaction between the fuel tube and the co-flow air is taken into account for our numerical model. This results in the better prediction of the temperature and the species profiles. Lastly, the input chemistry reaction mechanisms are also different; e.g. the hydrogen–oxygen submechanism of GRI2.11 containing nine species were utilised in Toro et al [1] while a full GRI3 reaction mechanism is utilised in this paper.

Comparing the appearance of all the flames in Figure 7a and b, it is found that there are many flames having the longer flame length but with the smaller flame size; for example, flame E is longer than flames C and D but its size is smaller. The flame width is found to play an important role in the compensation of the flame size for the shorter flame. This finding, therefore, can be used for explaining the trends of the chemistry heat release along with the flame temperature. As presented in Figure 8a-b, compensation of heat release is found from the flames having either the higher temperature or the flame size. At the similar flame temperature, the flames having the higher size generate higher heat release. In turn, the flame having the higher temperature produces the higher chemistry heat release.

Comparing the results presented in this paper with those of Dinesh et al. [8], who studied the turbulent flames of H_2/N_2 and H_2/CO , the effects of X_{H_2} on the flame temperature and the flame structure are found to be similar. However, this comparison result is not strong enough to imply that the effects of X_{H_2} on all the aspects of the flame characteristics presented in this paper would be same for both the laminar and turbulent H_2/N_2 flames. Therefore, further studies focusing investigation on the effects of X_{H_2} on the heat release and the emission formation at various flow condition (V_{avg}) of the turbulent H_2/N_2 flames are required in order to fulfil this gap.

Further study on the role of N_2 is also required. It can be seen on the comparison presented between the flames generated by the fuel having an equal H_2 content supplied into combustion (i.e. flames B and E) that the fuel stream containing a higher content of N_2 formulated the larger flame size, but with the lower flame temperature, chemistry heat release, and NO_x formation rate. A deeper understanding of the effect of N_2 on the flame

characteristics could therefore provide beneficial options in controlling the NO_x formation rate.

Regarding the concentration and production rate of NO_x, both rely strongly on the flame temperature, which is also the key factor affecting the increase or decrease of the chemistry heat release.

Furthermore, the study emphasised the role of X_{H_2} and V_{avg} that is not only the factors controlling the content of H₂ in the fuel stream but also controlling all the aspects of H₂/N₂ flame characteristics.

6 Conclusion

The effect of the H₂ content defined by the flow rate of H₂ on the various aspects of the flame characteristics of H₂/N₂ has been studied. The results presented revealed that the factors controlling the H₂ content in the fuel stream (X_{H_2} and V_{avg}) played an important role on the flame size, flame temperature, chemistry heat release, and NO_x emission. This finding can thus be potentially utilised for designing a suitable combustion system for this fuel.

During the analysis of the simulation results, the effect of N₂ was pointed out. It was shown that the fuel containing a higher content of N₂ generated the larger flame size, but with the lower flame temperature, chemistry heat release, and NO_x formation rate. Further study on this topic is also suggested since it could be capable of reducing the NO_x formation rate. Furthermore, as this study covers only the laminar diffusion flame, the flames of H₂ mixture in turbulent regime are also suggested as additional study in future.

Acknowledgement

The first author would like to thank Royal Thai Navy for funding his postgraduate research at the University of Glasgow.

7 Bibliography

- [1] V. V. Toro, A. V. Mokhov, H. B. Levinsky and M. D. Smooke, "Combined experimental and computational study of laminar, axisymmetric hydrogen–air diffusion flames," *Proceedings of the Combustion Institute*, vol. 30, no. 1, pp. 485-492, 2005.
- [2] K. Alex Francis, R. Sreenivasan and V. Raghavan, "Investigation of structures and reaction zones of methane-hydrogen laminar jet diffusion flames," *International Journal of Hydrogen Energy*, vol. 36, no. 17, pp. 11183-11194, 2011.
- [3] A. R. Choudhuri and S. R. Gollahalli, "Characteristics of hydrogen-hydrocarbon composite fuel turbulent jet flames," *International Journal of Hydrogen Energy*, vol. 28, no. 4, pp. 445-454, 2003.
- [4] A. R. Choudhuri and S. R. Gollahalli, "Combustion characteristics of hydrogen-hydrocarbon hybrid fuels," *International Journal of Hydrogen Energy*, vol. 25, no. 5, pp. 451-462, 2000.
- [5] L. Wu, N. Kobayashi, Z. Li, H. Huang and J. Li, "Emission and heat transfer characteristics of methane-hydrogen hybrid fuel laminar diffusion flame," *International Journal of Hydrogen Energy*, vol. 40, pp. 9579-9589, 2015.
- [6] J. Park, D. S. Bae, M. S. Cha, J. H. Yun, S. I. Keel, H. C. Cho, T. K. Kim and J. S. Ha, "Flame characteristics in H₂/CO synthetic gas diffusion flames diluted with CO₂: Effects of radiative heat loss and mixture composition," *international journal of hydrogen energy*, vol. 33, pp. 7256-7264, 2008.
- [7] J. Park, O. B. Kwon, J. H. Yun, S. I. Keel, H. Chang Cho and S. Kim, "Preferential diffusion effects on flame characteristics in H₂/CO syngas diffusion flames diluted with CO₂," *International Journal of Hydrogen Energy*, vol. 33, no. 23, pp. 7286-7294, 2008.
- [8] K. Ranga Dinesh, X. Jiang, M. Kirkpatrick and W. Malalasekera, "Combustion characteristics of H₂/N₂ and H₂/CO syngas nonpremixed flames," *International Journal of Hydrogen Energy*, vol. 37, no. 21, pp. 16186-16200, 2012.
- [9] Z. Wang, Y. Zhou, R. Whiddon, Y. He, K. Cen and Z. Li, "Investigation of NO formation in premixed adiabatic laminar flames of H₂/CO syngas and air by saturated laser-induced fluorescence and kinetic modeling," *Combustion and Flame*, vol. 164, pp. 283-293, 2016.

- [10] A. Frassoldati, T. Faravelli and E. Ranzi, "The ignition, combustion and flame structure of carbon monoxide/hydrogen mixtures. Note 1: Detailed kinetic modeling of syngas combustion also in presence of nitrogen compounds," *International Journal of Hydrogen Energy*, vol. 32, pp. 3471-3485, 2007.
- [11] C. Olm, I. G. Zsély, T. Varga, H. J. Curran and T. Turányi, "Comparison of the performance of several recent syngas combustion mechanisms," *Combustion and Flame*, vol. 162, no. 5, pp. 1793-1812, 2015.
- [12] G. P. Smith, D. M. Golden, M. Frenklach, N. W. Moriarty, B. Eiteneer, M. Goldenberg, C. T. Bowman, R. K. Hanson, S. Song, J. William C. Gardiner, V. V. Lissianski and a. Z. Qin, "GRI-mech 3.0," University of California at Berkeley, [Online]. Available: http://www.me.berkeley.edu/gri_mech/. [Accessed 11 August 2016].
- [13] A. Kéromnès, W. K. Metcalfe, K. A. Heufer, N. Donohoe, A. K. Das, C. J. Sung, J. Herzler, C. Naumann, P. Griebel, O. Mathieu, M. C. Krejci, E. L. Petersen, W. J. Pitz and H. J. Curran, "An experimental and detailed chemical kinetic modeling study of hydrogen and syngas mixture oxidation at elevated pressures," *Combust. Flame*, vol. 160, no. 6, pp. 995-1011, 2013.
- [14] S. G. Davis, V. J. Ameya, H. Wang and F. Egolfopoulos, "An optimized kinetic model of H₂/CO combustion," *Proceedings of the Combustion Institute*, vol. 30, no. 2005, pp. 1283-1292, 2005.
- [15] J. Li, Z. Zhao, A. Kazakov and M. Chaos, "A comprehensive kinetic mechanism for CO, CH₂O, and CH₃OH combustion," *International Journal of Chemical Kinetics*, vol. 39, no. 3, pp. 109-136, 2007.
- [16] M. P. Burke, M. Chaos, Y. Ju, F. L. Dryer and S. J. Klippenstein, "Comprehensive H₂/O₂ kinetic model for high-pressure combustion," *International Journal of Chemical Kinetics*, vol. 44, no. 7, pp. 444-474, 2011.
- [17] D. Healy, D. M. Kalitan, C. J. Auls, E. L. Petersen, G. Bourquel and H. J. Curran, "Oxidation of C₁-C₅ Alkane Quinary Natural Gas Mixtures at High Pressures," *Energy Fuels*, vol. 24, no. 3, pp. 1521-1528, 2010.
- [18] A. Kazakov and M. Frenklach, "Reduced Reaction Sets based on GRI-Mech 1.2," [Online]. Available: <http://combustion.berkeley.edu/drm/>. [Accessed 4 12 2017].
- [19] C. I. Heghes, "C₁-C₄ Hydrocarbon Oxidation Mechanism," [Online]. Available: <http://www.ub.uni-heidelberg.de/archiv/7379>. [Accessed 4 12 2014].
- [20] M. Fischer and X. Jiang, "An assessment of chemical kinetics for bio-syngas combustion," *Fuel*, vol. 137, pp. 293-305, 2014.
- [21] cd-adapco, "STAR CCM+ version 11 User guide," Cd-adapco, 2016. [Online]. Available: https://stevedocs.cd-adapco.com/starccmplus_latest_en/index.html?param=eNUMK.
- [22] J. Warnatz, U. Maas and R. W. Dibble, *Combustion: Physical and Chemical Fundamentals, Modeling and Simulation, Experiments, Pollutant Formation*, Berlin, Germany: Springer, 2006.
- [23] S. D. Cohen and A. C. Hindmarsh, "CVODE, A Stiff/Nonstiff ODE Solver in C," *Computers in Physics*, vol. 10, no. 2, pp. 138-143, 1996.

- [24] M. Ayoub, Rottier, S. C. Carpentier, C. Villermaux, A. M. Boukhalfa and D. Honor, "An experimental study of mild flameless combustion of methane/hydrogen mixtures," *International Journal of Hydrogen Energy*, vol. 37, no. 8, pp. 6912-6921, 2012.
- [25] G. Maragos, P. Rauwoens and B. Merci, "Assessment of a methodology to include differential diffusion in numerical simulations of a turbulent flame," *International Journal of Hydrogen Energy*, vol. 39, no. 25, pp. 13285-13291, 2014.
- [26] N. Peters and J. Warnatz, *Numerical Methods in Laminar Flame Propagation*, Springer-Verlag: A GAMM-Workshop, 2013.
- [27] E. S. Cho and S. H. Chung, "Numerical evaluation of NO_x mechanisms in methane-air counterflow premixed flames," *Journal of Mechanical Science and Technology*, vol. 23, no. 3, pp. 659-666, 2009.
- [28] P. Swarnkar, A. K. Sahu and T. Sundararajan, "Numerical study of effect of hydrogen content on the structure of syngas diffusion flame," in *10th International Conference on Heat Transfer, Fluid Mechanics and Thermodynamics*, Orlando, Florida, 2014.
- [29] R. J. Kee, D. Lewis, G. J. Warnatz, M. E. Coltrin and J. A. Miller, *A Fortran Computer Code Package For the Evaluation of Gas-Phase, Multicomponent Transport Properties*, Sandia National Labs, 1986.
- [30] A. Cuoci, A. Frassoldati, G. Buzzi Ferraris, T. Faravelli and E. Ranzi, "The ignition, combustion and flame structure of carbon monoxide/hydrogen mixtures. Note 2: Fluid dynamics and kinetic aspects of syngas combustion," *International Journal of Hydrogen Energy*, vol. 32, no. 15, pp. 3486-3500, 2007.
- [31] M. Arablu and E. Poursaeidi, "Using CFD for NO_x Emission Simulation in a Dual Fuel Boiler," *Combustion, Explosion, and Shock Waves*, vol. 47, no. 4, pp. 426-435, 2011.
- [32] P. Akridis and S. Rigopoulos, "Modelling of soot formation in a laminar coflow non-premixed flame with a detailed CFD-Population Balance model," *Procedia Engineering 102*, vol. 2015, pp. 1274-1283, 2015.
- [33] G. P. Smith, D. M. Golden, M. Frenklach, N. W. Moriarty, B. Eiteneer, M. Goldenberg, T. Bowman, R. K. Hanson, S. Song, W. C. Gardiner Jr., V. V. Lissianski and Z. Qin. [Online]. Available: http://www.me.berkeley.edu/gri_mech/. [Accessed 4 12 2017].

Nomenclature

Uppercase letters	Lowercase letters
C_v Contribution to the molar specific heat of each specie	a_k Weight factor
$D_{i,t}$ Thermal diffusion coefficient	g Gravitational acceleration
D_m Molecular diffusivity of multi component gases	h Specific enthalpy
$D_{i,m}$ Binary diffusion of component i and m	k Thermal conductivity coefficient
$F_{k,j}$ Diffusive flux component	p Pressure
\vec{J} Diffusive flux	r Radial coordinate
K_k Absorption coefficient of each grey gases	v Velocity
S_h Heat due to chemical reaction and radiation	\dot{v} Volume flow rate
K Total number of grey gases	
M Molecular weight	Subscripts
S Optical path length	i component i
T Temperature	j Specie j
T^* Reduced temperature	k Specie k
V Velocity of fuel and air	m Multi component or component m
X Mole fraction	x Component in axial direction
Y Mass fraction	r Component in radial direction
	$tran$ Translation
Greek letters	rot Rotation
ρ Fluid density	vib Vibration
σ Collision diameter	avg Average
$\bar{\tau}$ Viscous stress tensor	max maximum
μ Molecular viscosity	
ω Production rate of each specie	Abbreviations
	CVODE A package written in C for solving differential equation
	DARSCFD Digital analysis of reaction

Ω	Collision integral	systems
----------	--------------------	---------

Table 1 Summary of published papers relating to the study of effect of hydrogen concentration on flame characteristics

Sources	Configuration	Fuel	H ₂ volume fraction (%)	Method
Francis et al. [2]	Co-flow laminar diffusion flame	H ₂ /CH ₄	0 - 80	Experiment; CFD
Ayoub et al. [24]	Mild flameless combustion	H ₂ /CH ₄	0 - 100	Experiment
Wu et al. [5]	Co-flow laminar diffusion flame	H ₂ /CH ₄	0 - 50	Experiment
Choudhuri et al. [4]	Laminar diffusion flame	H ₂ /natural gas; H ₂ /C ₃ H ₈	65, 80, 100	Experiment
Choudhuri et al. [3]	Turbulent diffusion confined flam	H ₂ /natural gas	0 -35	Experiment
Park et al. [6]	Counter flow diffusion flame	H ₂ /CO	20, 80	Numerical method (CHEMKIN)
Dinesh et al. [8]	Turbulent diffusion flame	H ₂ /CO; H ₂ /N ₂	75, 50, 30	CFD
Toro et al. [1]	Laminar diffusion flame	H ₂ /N ₂	50	Experiment; CFD

Table 2 Details of mesh generation for mesh dependency test

Resolution	Levels from outer of fuel outlet tube to axis	Levels from outer of fuel outlet tube to top plane	Levels from outer of fuel outlet tube to left plane	Levels from outer of fuel outlet tube to top plane	Total number of cells	Smallest cells size (mm)
Coarse	10	50	25	12	2880	0.5
Normal	16	100	50	24	7800	0.2
Fine	20	200	200	32	26000	0.1

Table 3 Composition, volume flow, and velocity of fuel and air of all simulated flames

Flame	X_{H_2}	X_{N_2}	V_{avg} (ms^{-1})	\dot{v}_{H_2} (cm^3s^{-1})	\dot{v}_{N_2} (cm^3s^{-1})	\dot{v}_{total} (cm^3s^{-1})
Flame A	0.25	0.75	0.25	3.97	11.93	15.9
Flame B	0.5	0.5	0.25	7.95	7.95	15.9
Flame C	0.75	0.25	0.25	11.93	3.97	15.9
Flame D	1	0	0.25	15.9	0	15.9
Flame E	0.25	0.75	0.5	7.95	23.85	31.8
Flame F	0.5	0.5	0.5	15.9	15.9	31.8
Flame G	0.75	0.25	0.5	23.85	7.95	31.8
Flame H	1	0	0.5	31.8	0	31.8
Flame I	0.25	0.75	0.75	11.93	35.77	47.7
Flame J	0.5	0.5	0.75	23.85	23.85	47.7
Flame K	0.75	0.25	0.75	35.77	11.93	47.7
Flame L	1	0	0.75	47.7	0	47.7

Table 4 Category of flames

Resolution	Enrich N_2	Equal H_2/N_2	Enrich H_2	Pure H_2	V_{avg} (ms^{-1})
Flame set I	A	B	C	D	0.25
Flame set II	E	F	G	H	0.5
Flame set III	I	J	K	L	0.75
X_{H_2}	0.25	0.5	0.75	1	1

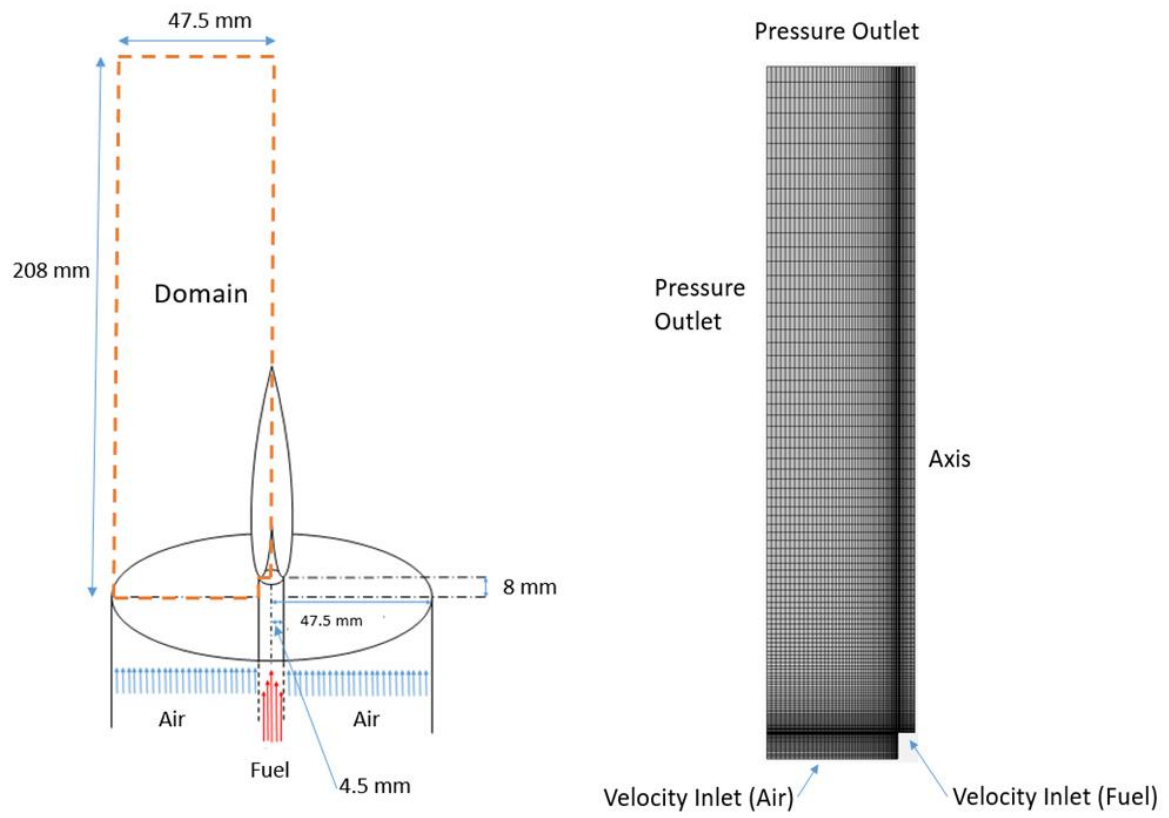


Figure 1 Left: Physical appearance and dimension of the burner; Right: Generated mesh (normal) and boundary condition of each plane

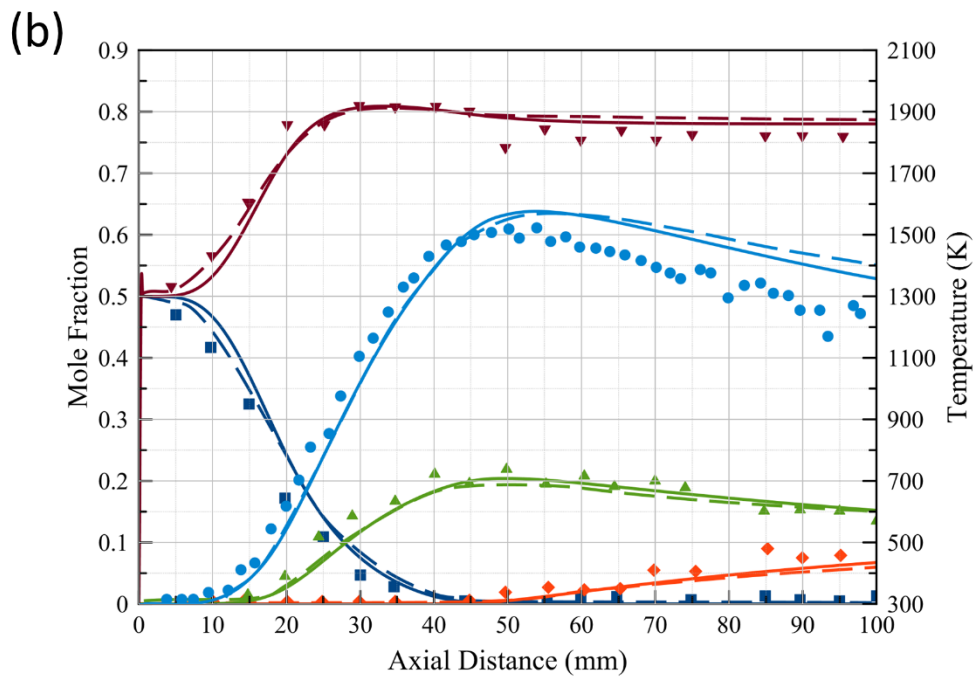
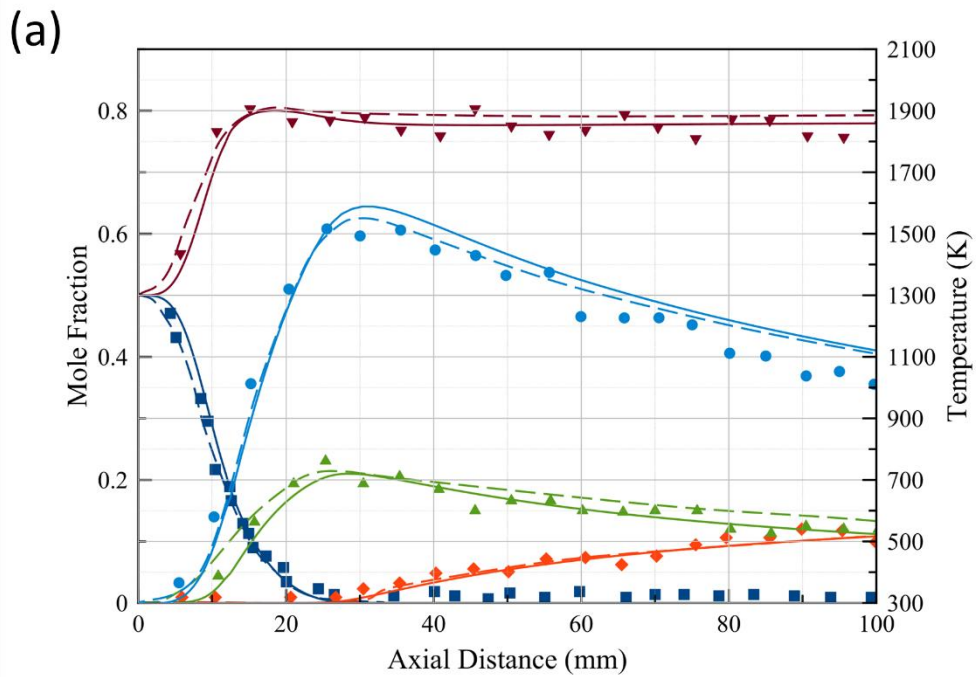


Figure 2 Axial temperature and species profiles of flame having an equal mole fraction of H₂ and N₂ at V_{avg} of 0.27 ms⁻¹ (a), and 0.5 ms⁻¹ (b)

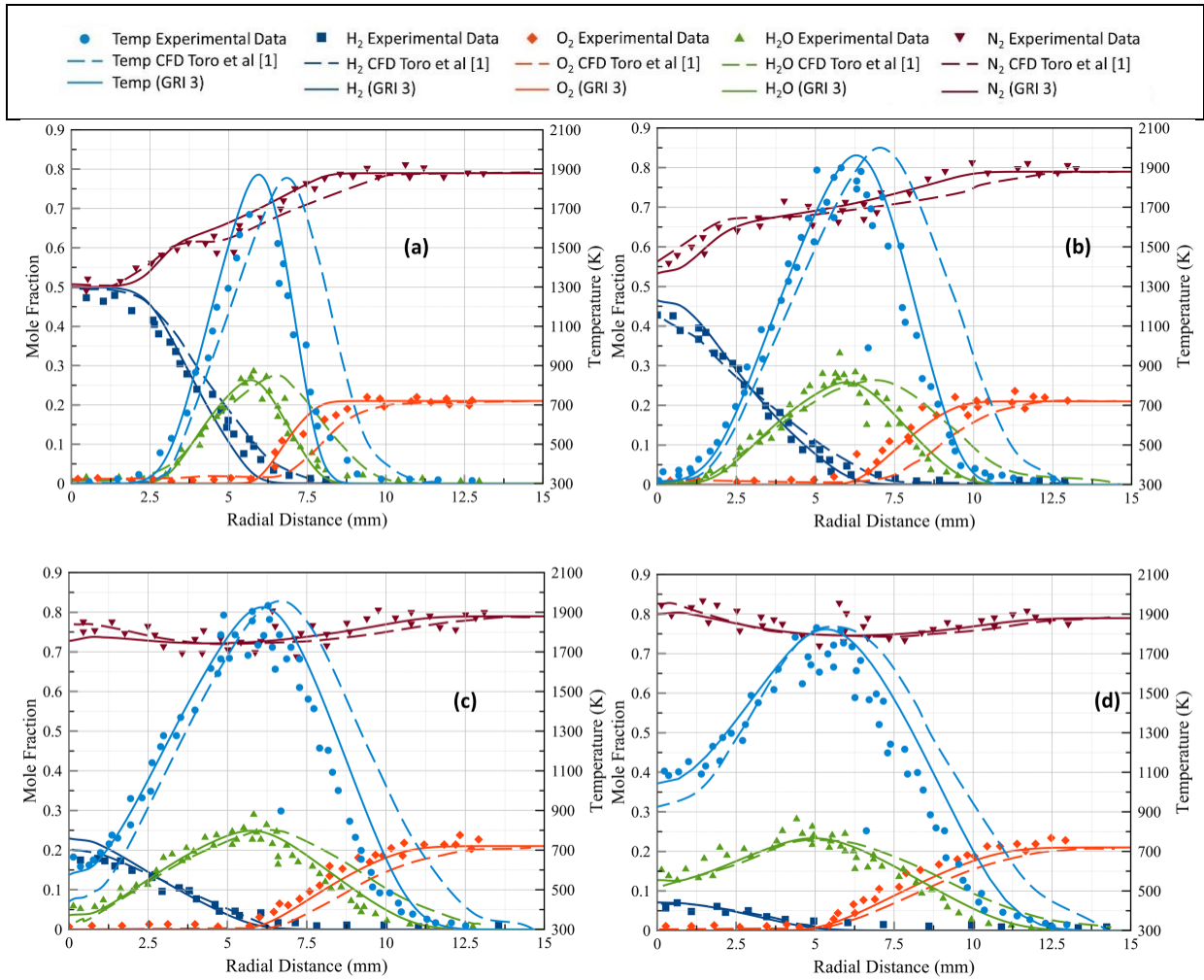


Figure 3 Radial temperature and species profiles at (a) 3 mm (b) 10 mm (c) 20 mm and (d) 30 mm above the burner of flame having an equal mole fraction of H₂ and N₂ at V_{avg} of 0.5 ms⁻¹

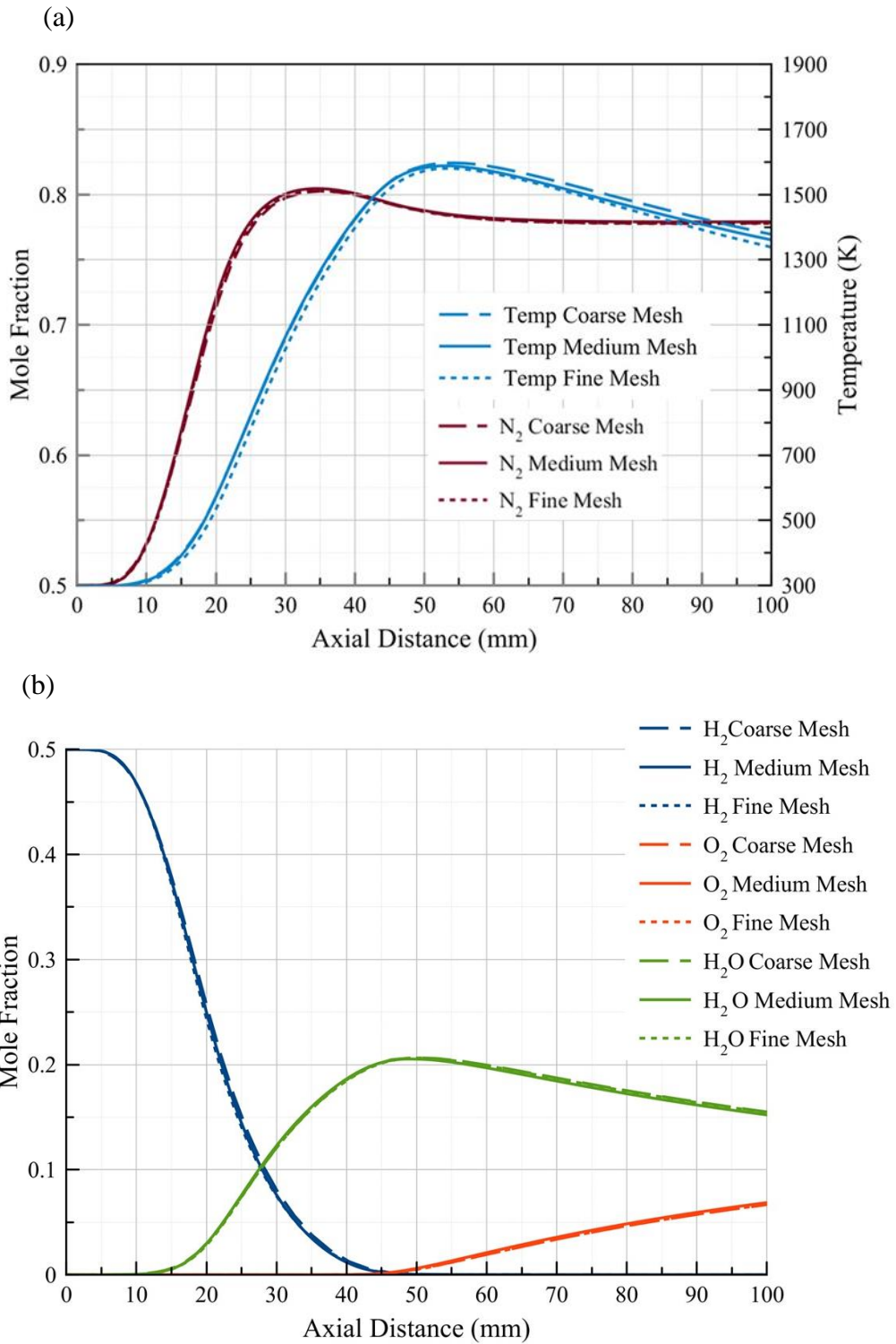


Figure 4 Results of the mesh dependency test on (a) the profiles of N_2 and temperature; (b) the profiles of H_2 , O_2 , and H_2O

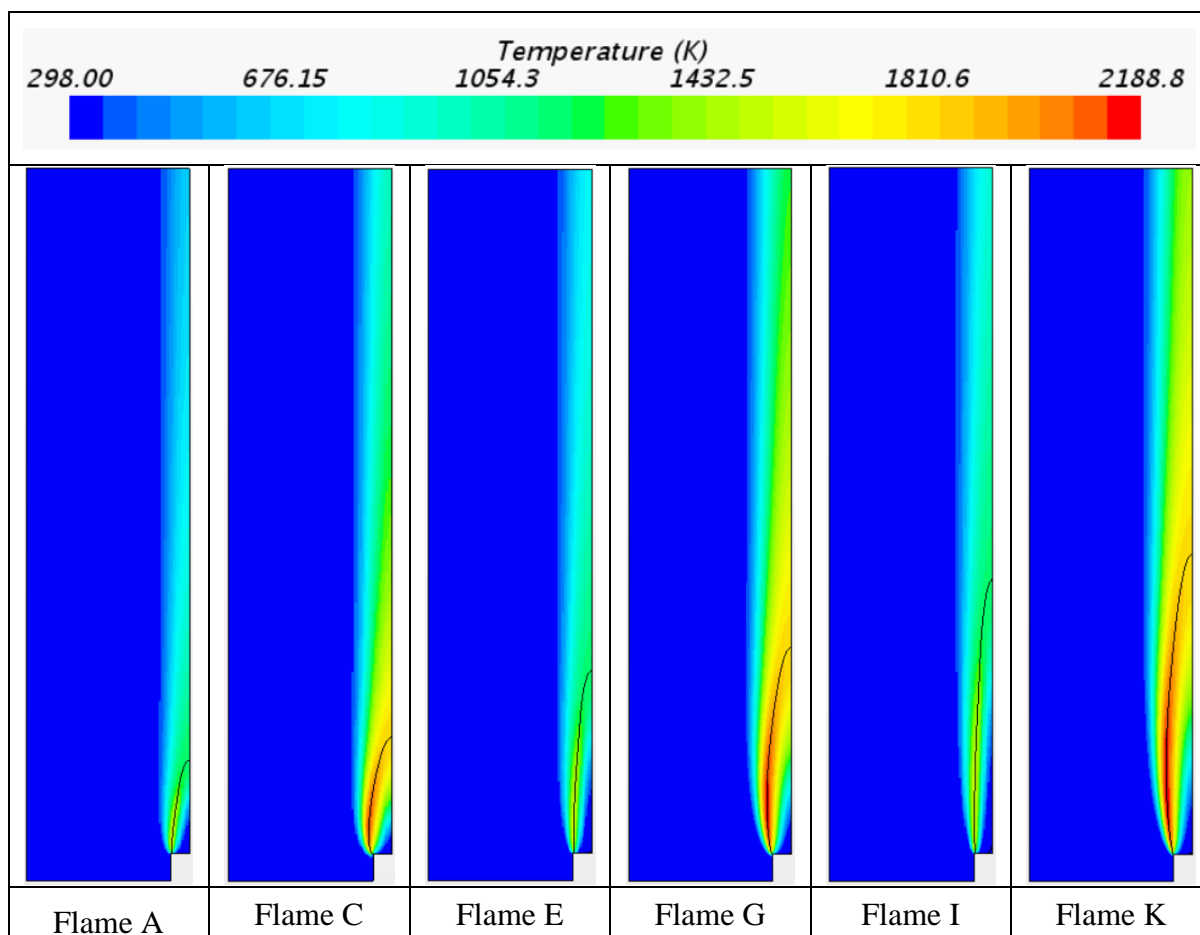


Figure 5 Temperature contours of the N₂ or H₂ rich flames at various flow conditions

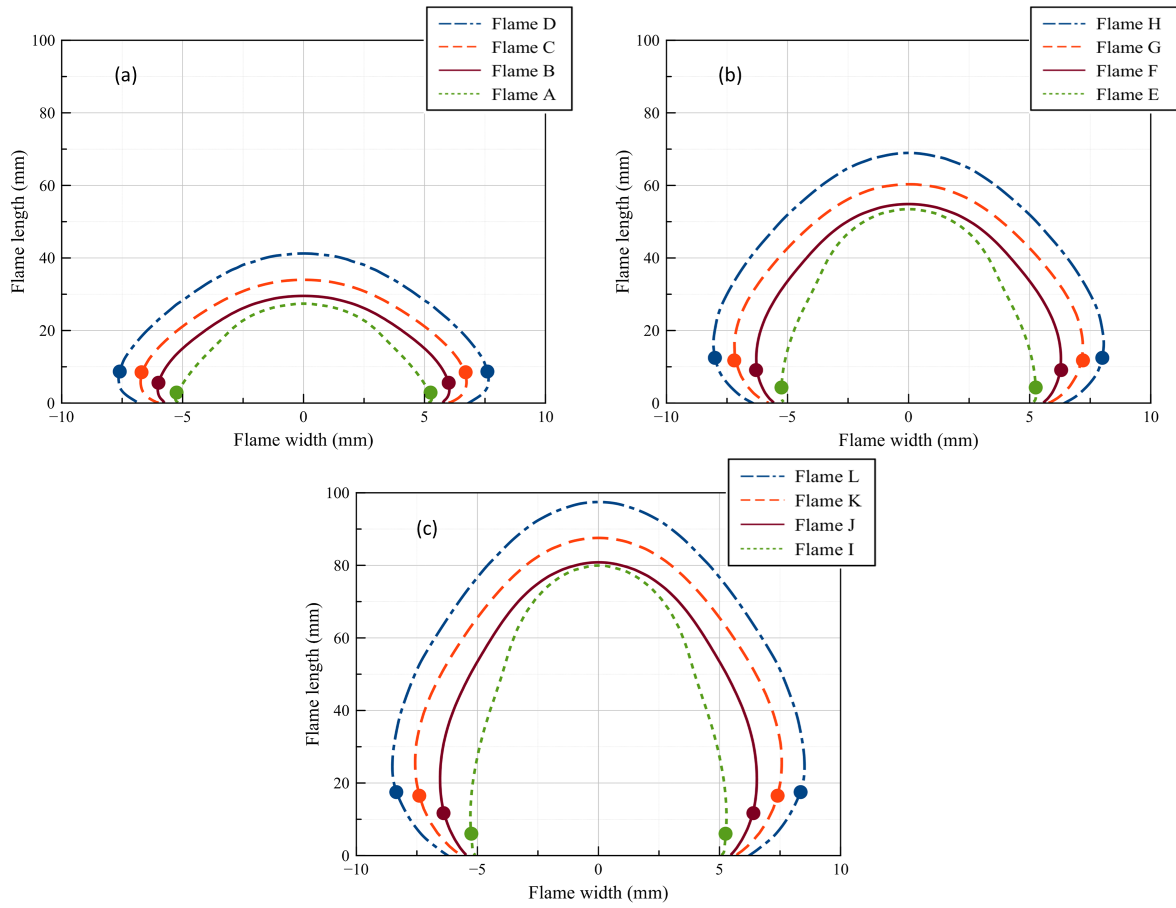
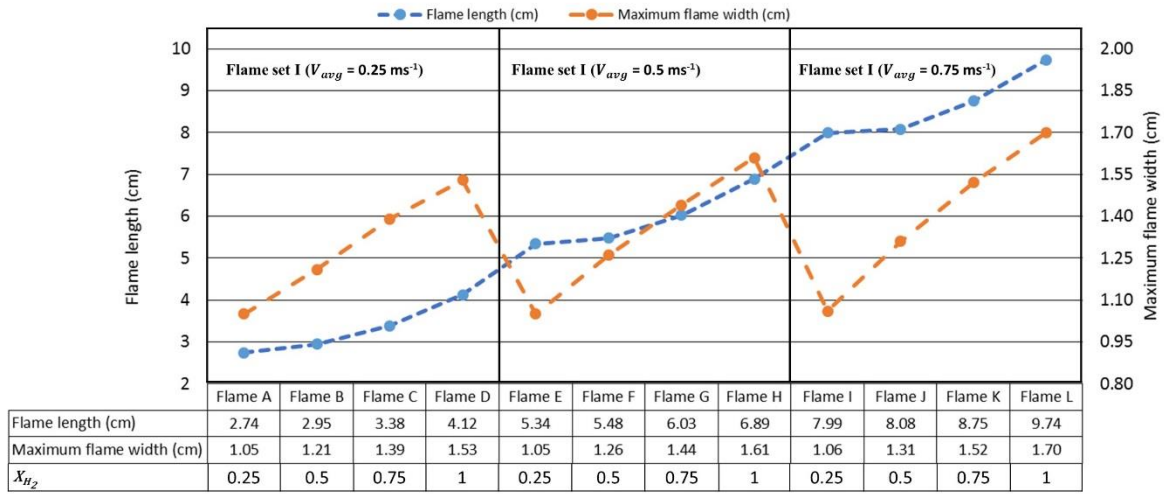


Figure 6 Illustration of the flame dimension through an approximated flame front line in different flow conditions: (a) $V_{avg} = 0.25 \text{ ms}^{-1}$, (b) $V_{avg} = 0.5 \text{ ms}^{-1}$, and (c) $V_{avg} = 0.75 \text{ ms}^{-1}$

(a)



(b)

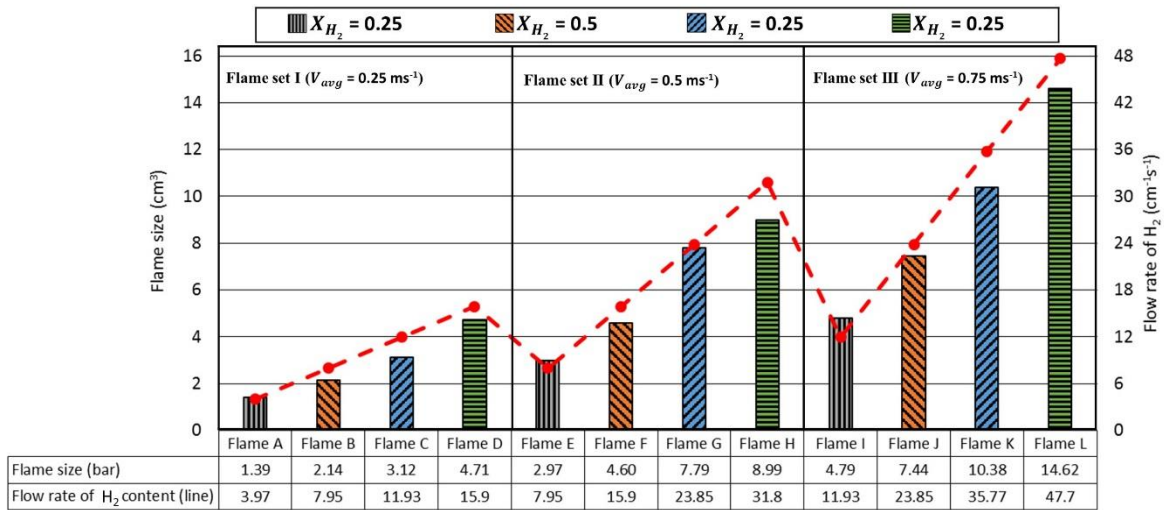
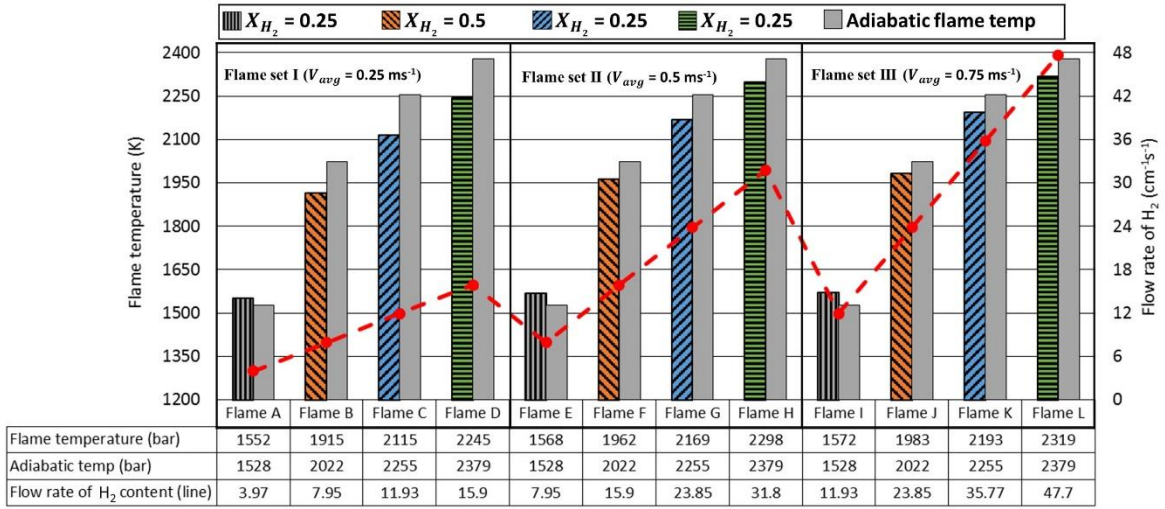


Figure 7 (a) Flame length and maximum flame width; (b) Flame size and volume flow rate of H_2

(a)



(b)

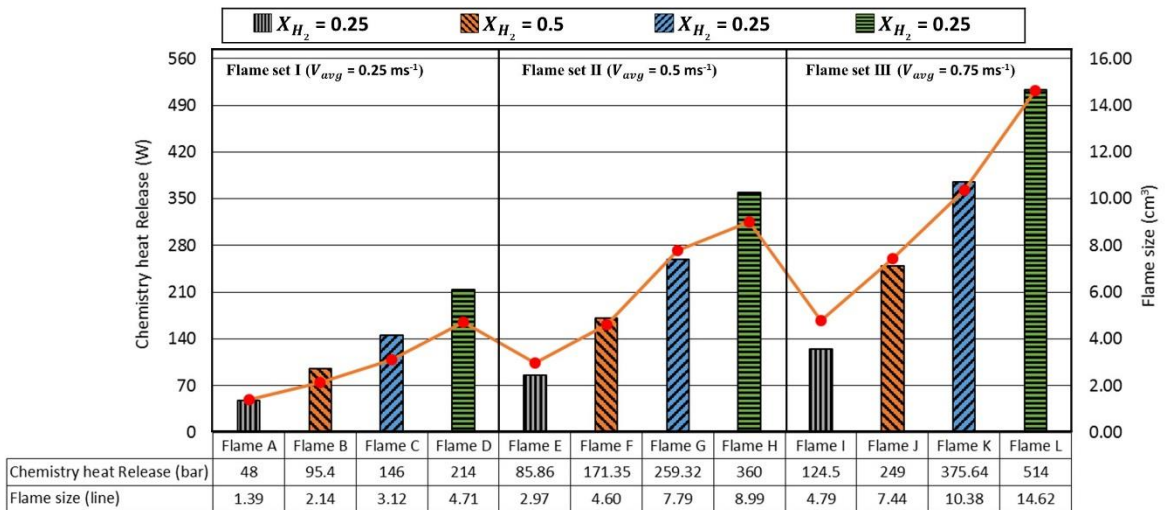


Figure 8 (a) Flame temperature, adiabatic flame temperature, and flow rate of H₂ content; (b) Chemistry heat release of all flames and flame size

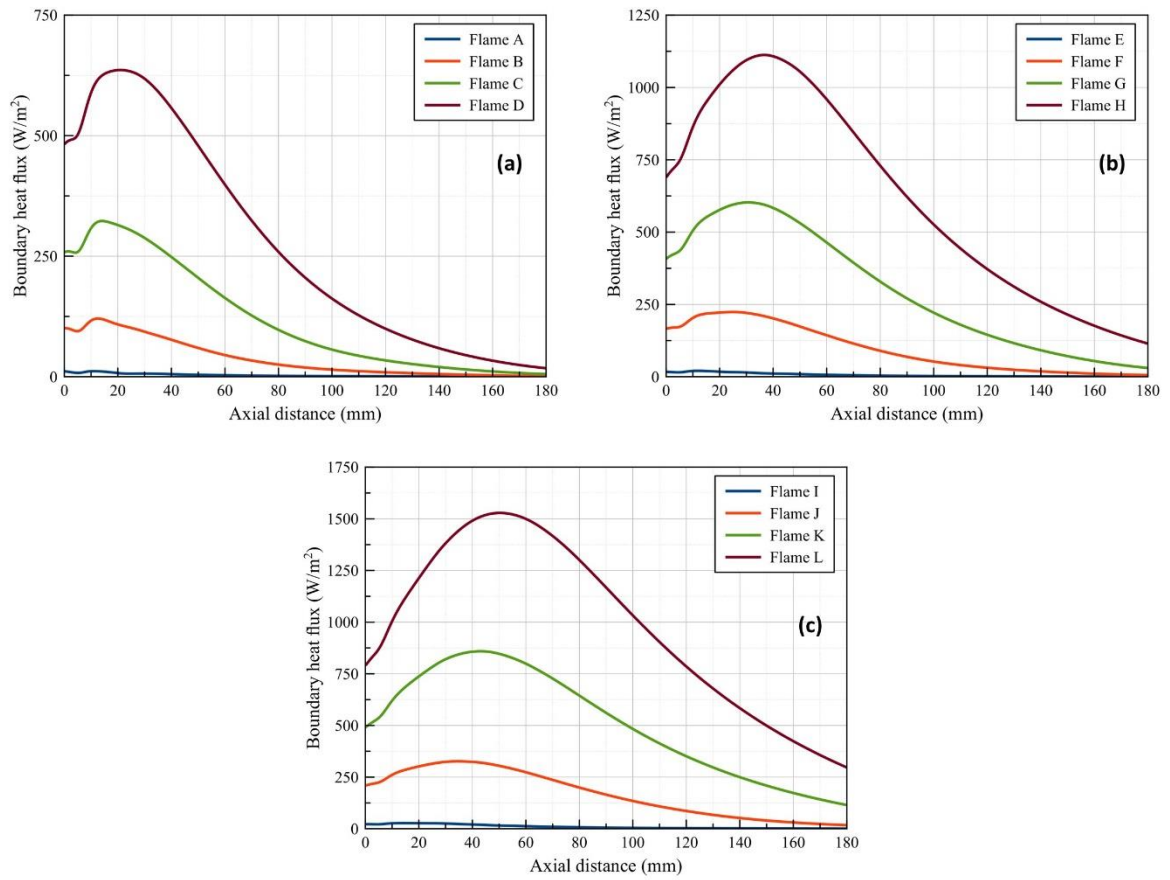


Figure 9 Boundary heat flux of all flames (a) flames in flame set I, (b) flames in flame set II (c) flames in flame set III

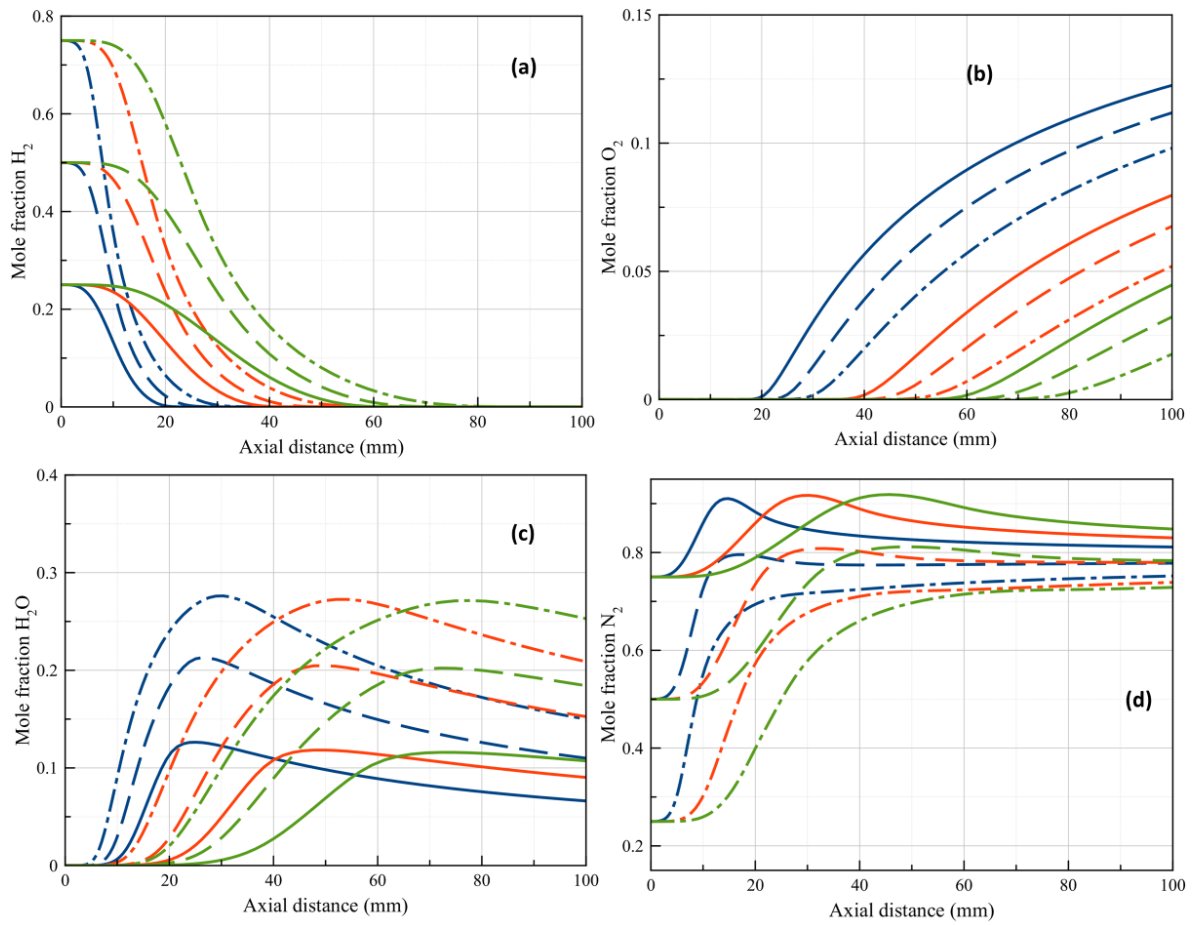
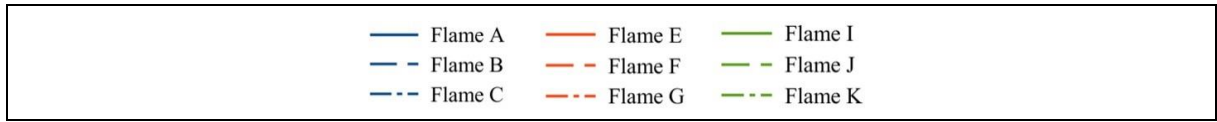


Figure 10 Species axial profiles of all the simulated flames (a) H₂; (b) O₂; (c) H₂O; (d) N₂

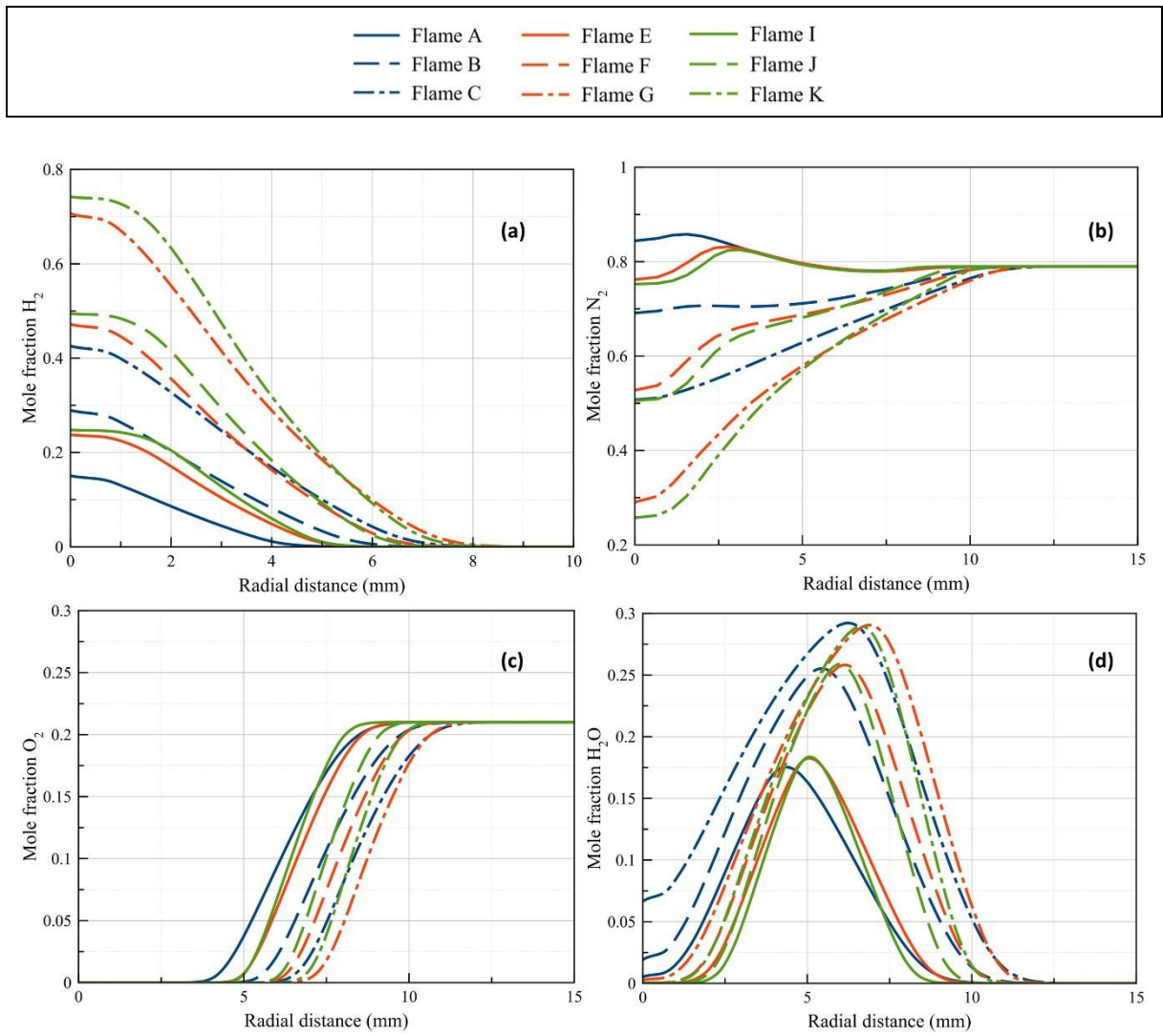


Figure 11 Species radial profiles at 9 mm above fuel exit of all the simulated flames (a) H_2 ; (b) O_2 ; (c) H_2O ; (d) N_2

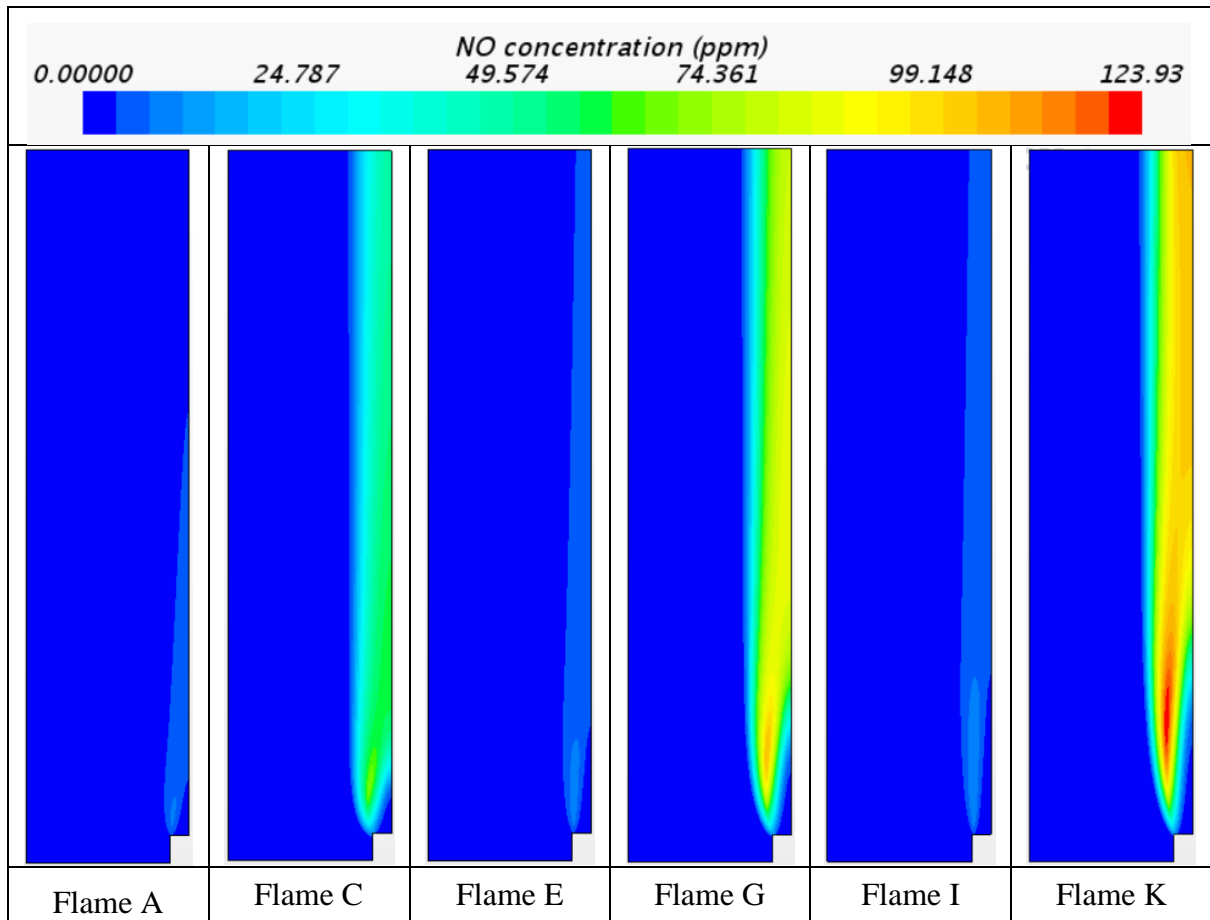
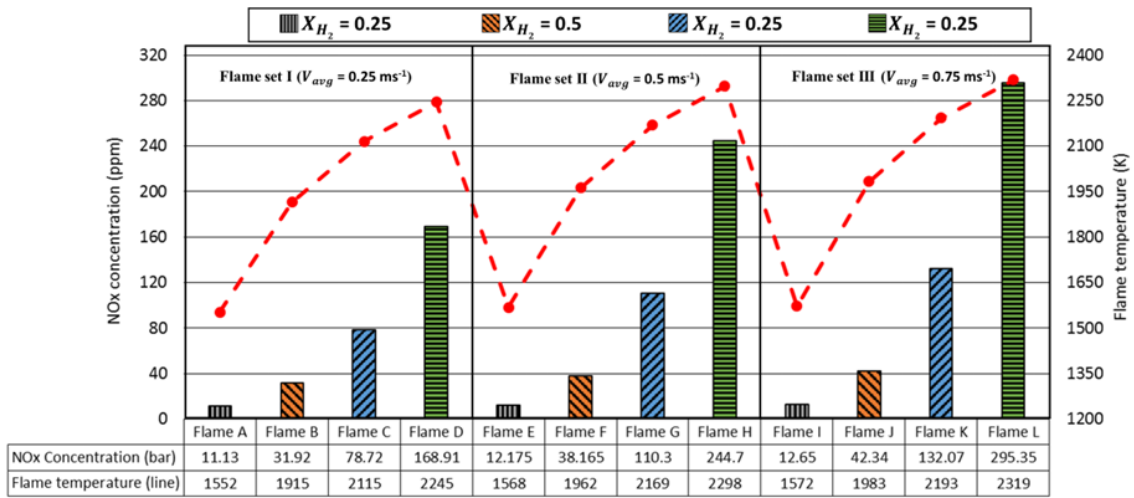


Figure 12 Contour plots of the concentration of NO_x of enrich H₂ and enrich N₂ flames

(a)



(b)

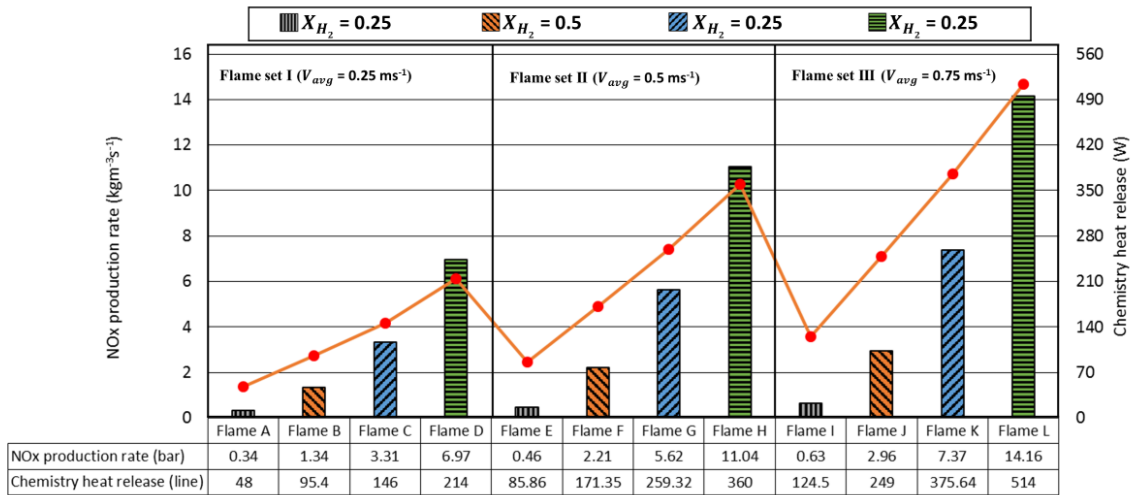


Figure 13 (a) Maximum concentration of NOx and maximum H₂ temperature; (b) NOx production rate and H₂ content